

# Self-Powered e-Skin Based on Integrated Flexible Organic Photovoltaics and Transparent Touch Sensors

Nitheesh M. Nair, Dhayalan Shakthivel, Kumar M. Panidhara, Varun Adiga, Praveen C Ramamurthy, and Ravinder Dahiya\*

There is a growing interest in the large area, lightweight, low-power electronic skin (e-Skin), consisting of a multitude of sensors over conformable surfaces. The use of multifunctional sensors is always challenging, especially when their energy requirements are considered. Herein, the heterogeneous integration of custom-made flexible organic photovoltaic (OPV) cells is demonstrated with a large area touch sensor array. The OPV can offer power density of more than  $0.32 \mu\text{W cm}^{-2}$  at 1500 lux, which is sufficient to meet the instantaneous demand of the array of touch sensors. In addition to energy harvesting, it is shown that the OPVs can perform shadow sensing for proximity and gesture recognition, which are crucial features needed in the e-Skin, particularly for safe interaction in the industrial domain. Along with pressure sensing (sensitivity of up to  $0.26 \text{ kPa}^{-1}$  in the range of 1–10 kPa) and spatial information, the touch sensors made of indium tin oxide and monolayer graphene have shown  $>70\%$  transparency, which allow light to pass through them to reach the bottom OPV layer. With better resource management and space utilization, the presented stacked integration of transparent touch-sensing layer and OPVs can evolve into a futuristic energy-autonomous e-Skin that can “see” and “feel.”

## 1. Introduction

Electronic skin (e-Skin) is a critical interface needed in robotics, prosthetics, and health monitoring applications, etc., to enable safe interaction or to gather relevant data by allowing to receive tactile or pressure information from large areas.<sup>[1]</sup> A large number of multifunctional sensors, including pressure, proximity, temperature, and strain, etc., are needed in the e-Skin along with the readout electronics—all of which require considerable energy for autonomous operation over an extended period. The existing approaches to power the devices in the e-Skin include using batteries,<sup>[2]</sup> fuel cells,<sup>[3]</sup> mains supply (depending on application) or using energy harvesters based on different mechanisms such as photovoltaics (PVs), piezoelectric,<sup>[4]</sup> pyroelectric,<sup>[5]</sup> triboelectric,<sup>[6]</sup> and thermoelectric,<sup>[7]</sup> etc. The restricted-energy budget, which results in a shorter

operational time, bulkiness, non-flexible, and nonconformability, are some of the shortcomings of the batteries. The localized energy generation with various energy harvesters also suffers from a limited energy budget. Except for PV devices, most of the harvesters generate energy in the mW range and lower<sup>[8]</sup> and for this reason maybe many of the harvesters are also used as active sensors.<sup>[6]</sup>


With the ability to transform incoming photons or ambient light into electrical energy, the PV devices can generate energy in the order of hundreds of mW, which is sufficient for the operation of several sensors and hence for the e-Skin. The generated energy can either be utilized to directly power the sensors and associated electronics<sup>[8,9]</sup> or stored in devices such as supercapacitors or batteries and used when there is no light.<sup>[10]</sup> The technique of ambient light detection facilitates the monitoring of shadows produced by approaching objects or human hands, which may then be interpreted to extract proximity and gesture information for robotic automation. PVs has been utilized in various sensing applications such as visible light sensing,<sup>[11]</sup> gesture recognition,<sup>[12]</sup> localization, and positioning.<sup>[13]</sup> Si solar-cell-based e-Skin or solar skin was demonstrated recently, which can produce surplus energy of 380 mW from a palm-sized area and can also function as a tactile sensor with shadow and proximity-sensing capabilities.<sup>[14]</sup> The foreseeable challenges to expanding the commercial Si-based PVs for energy-autonomous e-Skin come from their brittle property, limited flexibility, areal

N. M. Nair, D. Shakthivel  
James Watt School of Engineering  
University of Glasgow  
Glasgow G12 8QQ, UK

K. M. Panidhara  
Materials Engineering Department  
Indian Institute of Science Bangalore  
Bangalore 560012, India

V. Adiga, P. C. Ramamurthy  
Interdisciplinary Centre for Energy Research  
Indian Institute of Science Bangalore  
Bangalore 560012, India

R. Dahiya  
Bendable Electronics & Sustainable Technologies (BEST) Group  
Northeastern University  
Boston, MA 02115, USA  
E-mail: r.dahiya@northeastern.edu

 The ORCID identification number(s) for the author(s) of this article can be found under <https://doi.org/10.1002/aisy.202300103>.

© 2023 The Authors. Advanced Intelligent Systems published by Wiley-VCH GmbH. This is an open access article under the terms of the Creative Commons Attribution License, which permits use, distribution and reproduction in any medium, provided the original work is properly cited.

DOI: 10.1002/aisy.202300103

restriction, cost of fabrication, and the end-of-life difficulties related to disposal as e-waste.<sup>[15]</sup> However, most of the applications mentioned earlier require e-Skin to be ultra-flexible, and therefore, there is a need to advance these solutions for energy-autonomous e-Skin. These shortcomings are straightforward to address using organic PVs (OPVs) due to the affordable cost, simplified and robust cell designs, feasibility for the large area using simple wet synthesis techniques and inherent materials flexibility.<sup>[16]</sup> Hence, the current work uses OPVs to develop energy autonomous e-Skin.

In this article, we present a new approach where custom-made OPVs are heterogeneously integrated with transparent touch sensors to realize an e-Skin that can generate its own energy. We adopted OPVs as the base layer of the e-Skin, which can generate energy as well as function as sensors. The OPV generates energy when light falls on its surface, at the same time, if an approaching object hinders light from reaching the OPV, the amount of energy generated will decrease and eventually become zero when it comes into contact with the surface. These variations in energy generation are monitored for sensing the shadows and proximity. This approach has huge potential for shape identification and gesture-recognition capability of e-Skin.

Further, a transparent touch sensor array, fabricated by a simple mechanical patterning technique, was integrated on the top of OPVs for touch or pressure-sensing applications. Being transparent, the touch sensors allow the light to reach the OPVs for sensing and power generation. Transparent electronic devices and sensors have been extensively researched in recent years due to their applications in energy devices,<sup>[17]</sup> sensing,<sup>[18]</sup> displays,<sup>[19]</sup> etc. A wide variety of materials, including indium tin oxide (ITO),<sup>[20]</sup> graphene,<sup>[21]</sup> metallic nanowires,<sup>[22]</sup> and polymers,<sup>[23]</sup> have been explored as transparent conductors. Here, two types of touch sensors were fabricated: a) ITO-based and b) monolayer graphene-based. Both have the interdigitated coplanar structure and transparent dielectric, polydimethylsiloxane (PDMS), as the top dielectric. The graphene-based sensor showed reduced sensitivity ( $0.006 \text{ kPa}^{-1}$ ) but was nearly consistent over the pressure range of 10–60 kPa, as contrasted to the ITO-based sensor's highest response of  $0.255 \text{ kPa}^{-1}$  between the 0 and 10 kPa pressure domain. This demonstration of the energy-autonomous e-Skin prototype, with distributed energy generation and better resource utilization, could pave the way for new directions power management in e-Skin and robotics.

## 2. Results and Discussion

### 2.1. OPV Fabrication and Characterization

An OPV cell typically converts the incident photons into electrical current or photocurrent and its efficiency is determined by the absorption coefficient of the active layer, the conversion rate of photons into charge carriers (electrons and holes), and the separation of charge carriers which are swept into external circuitry. The generated current density of OPV is a measure of solar cell efficiency and it is also linearly related to the intensity of light in the environment. The OPV cells used in this work consist of a bulk heterojunction configuration, where a donor,

poly[4,8-bis(5-(2-ethylhexyl)thiophen-2-yl)benzo[1,2-b;4,5-b']-dithiophene-2,6-diyl-alt-(4-(2-ethylhexyl)-3-fluorothieno[3,4b]thiophene)-2-carboxylate-2,6-diyl] (PTB7-Th), and acceptor materials, [6,6]-phenyl C71-butyric acid methyl ester (PC<sub>71</sub>BM), blend to form the active layer.<sup>[24]</sup> PTB7-Th:PC<sub>71</sub>BM has recently received considerable interest due to its low cost, low temperature, and solution processability, scalability, and compatibility with flexible substrates.<sup>[25]</sup> PTB7-Th:PC<sub>71</sub>BM-based solar cells offer better efficiency under white light emitting diode (LED) indoor illumination conditions in comparison to commercial c-Si solar cells.<sup>[26]</sup> Features like lightweight, mechanical flexibility, and stability make it a good choice of material for the energy autonomous e-Skins. ZnO and MoO<sub>3</sub> compounds were used as the hole and electron collectors, respectively, for efficient carrier separation from the active layer and Ag, and ITO is used as the electrodes for the carrier collection at both the terminals, with the device fabricated on a flexible polyethylene terephthalate (PET) substrate. **Figure 1a** shows the schematic of individual layers of the OPV.

**Figure 1b** shows the electrical characteristics of the OPV, under AM1.5G, and **Figure 1c** shows the corresponding maximum generated power ( $P_{\text{MAX}}$ ). The OPV exhibited an open-circuit voltage ( $V_{\text{OC}}$ ) of 750 mV and a short-circuit current density ( $J_{\text{SC}}$ ) of  $2.48 \text{ mA cm}^{-2}$ , with a  $P_{\text{MAX}}$  of  $0.86 \text{ mW cm}^{-2}$ . The OPV exhibited a fill factor of 46.4% with 0.86% power conversion efficiency. The solar cell resembles a diode junction when it is not illuminated, and the current density–voltage ( $J$ – $V$ ) curve is altered when the light falls on the OPV and it starts to produce electricity. The amount of shift with increasing light intensity is prominent as more photocurrent is generated. **Figure 2** depicts the electrical characteristics of the cell with respect to the different light intensities and is tabulated in Table S1, Supporting Information. Cell parameters such as  $J_{\text{SC}}$ ,  $V_{\text{OC}}$ , and  $P_{\text{MAX}}$  were observed to increase with light intensity. Values of  $J_{\text{SC}}$  and  $P_{\text{MAX}}$  were observed to be monotonically increasing with all light intensities, while the rate of  $V_{\text{OC}}$  increase at high intensities was observed to be lesser compared to the values at low intensities, which is dominated by bi- and monomolecular recombination mechanisms.<sup>[27]</sup> Hence, the variation in  $V_{\text{OC}}$  is less sensitive to higher light intensities compared to  $J_{\text{SC}}$ .<sup>[28]</sup> Interior lighting conditions are quite different from outdoor lighting since the light intensity is typically orders of magnitude lower and the spectra of indoor lighting sources differ significantly from those of solar emission.<sup>[29]</sup> Generally, standard indoor illumination intensities are limited to 3000 lux, within this region, the variation in  $V_{\text{OC}}$  can also be assumed monotonic. These differences in electrical performance with illumination can be used to fulfill the sensing capabilities of e-Skins, such as shadow and proximity detection. The encapsulated OPV demonstrated good storage stability, and performance degradation was negligible even after 5 months storage under ambient conditions (see **Figure S1**, Supporting Information).

#### 2.1.1. Shadow and Proximity Sensing Using PVs

Under a specific illumination, the OPV will generate a steady photocurrent/photovoltage at a given load. The illumination, and thereby the generated current gets diminished when an opaque object comes between the source of light and the OPV.

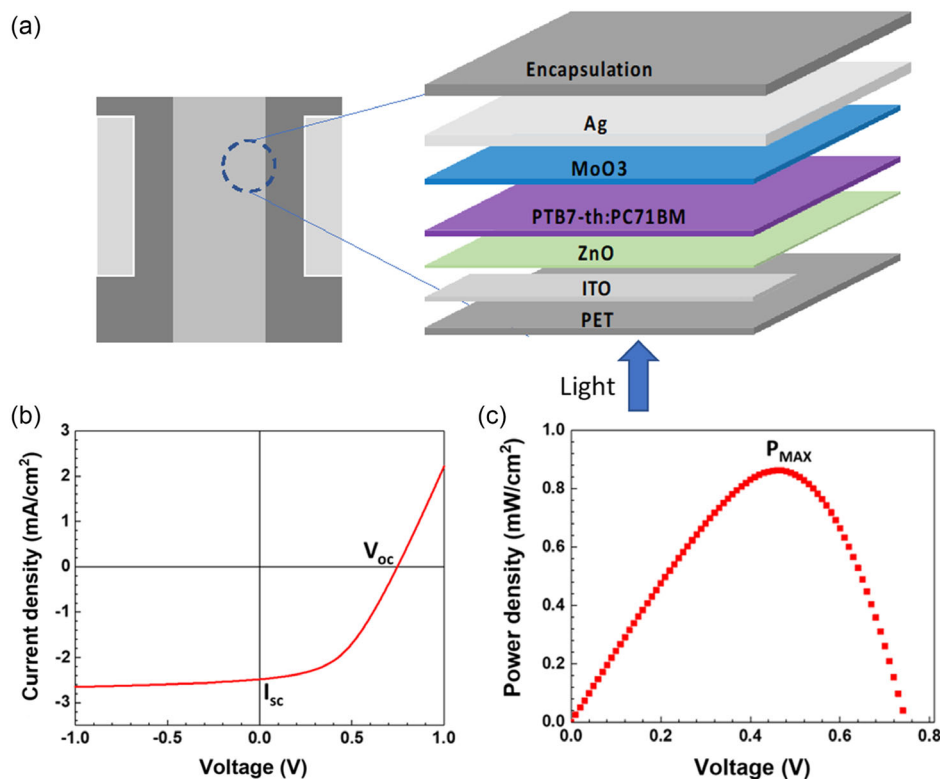


**Figure 1.** Organic photovoltaic (OPV) characterization. a) Schematic showing the individual layers of the OPVs. OPV cell characterization under AM1.5 G showing the relations between b) current and c) power densities with respect to voltage.

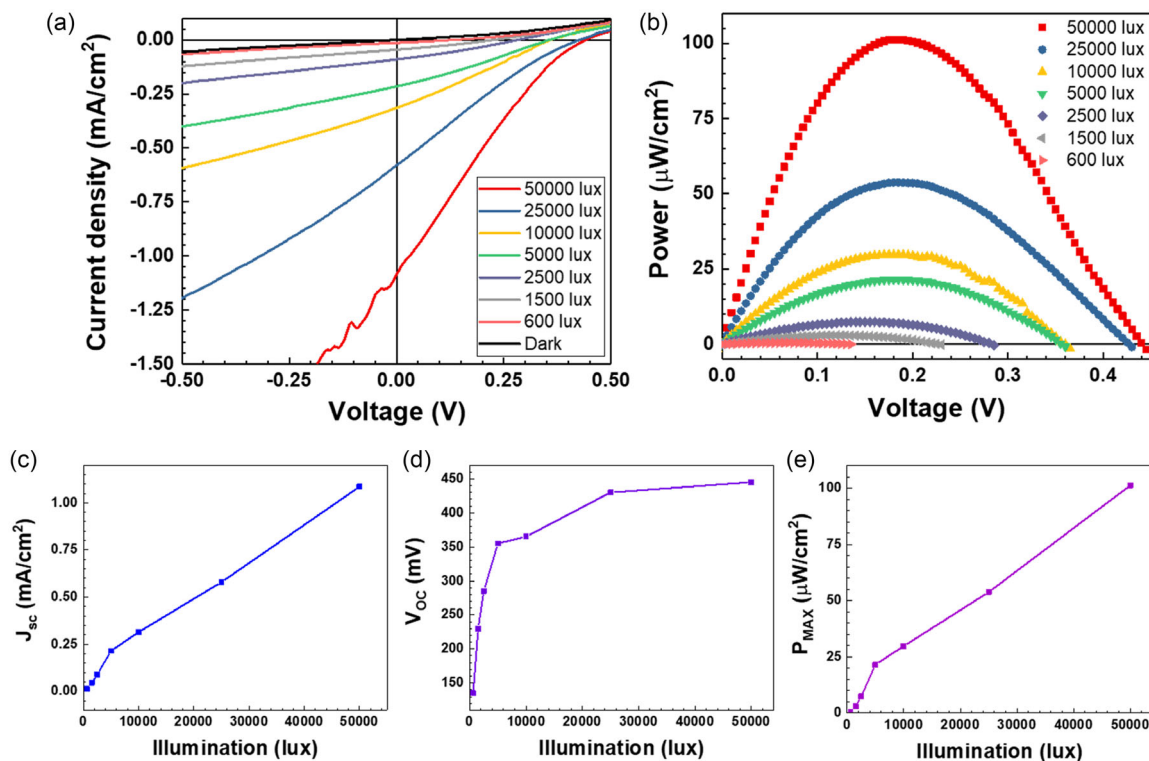


**Figure 2.** Light intensity dependence of the OPV parameters. The variation in a) current–voltage ( $I$ – $V$ ) and b) photovoltaics (PV) characteristics of OPV with illumination. c) Short-circuit current density,  $J_{SC}$ , d) open-circuit voltage,  $V_{OC}$ , and e) maximum generated power density,  $P_{MAX}$ .

Due to the blocking of the illumination, the shadow gets denser as the object comes closer to the OPV, and when it is about to touch the OPV, the created photovoltage will go down to zero. Hence, it is possible to gather data for edge detection, shape assessment, and proximity detection by collecting, combining, and analyzing the output current of the OPV cell.

**Figure 3** demonstrates a single OPV operating in the proximity-sensing mode. The OPV produces a steady-state output when exposed to the environment having 600 lux of white light illumination. When an object approaches the OPV, the generated voltage reduces due to the shadow casting and finally diminishes to 0 mV when about to touch the OPV. The OPV response exhibited good repeatability and fast response. Since the illumination level dynamically depends on the environmental conditions, the OPV response can be normalized with respect to the maximum generated voltage at a given illumination.

### 2.1.2. Gesture Recognition using PVs

Sensing human gestures is considered as one of the natural ways of understanding human interaction and communication. A wide variety of sensors employed for this purpose include electromagnetic sensors,<sup>[30]</sup> acoustic- and ultrasound-based sensors,<sup>[31]</sup> accelerometer-based sensors,<sup>[32]</sup> cameras,<sup>[33]</sup> and light sensors. The major challenges associated with these sensors are that they require additional space for installation and depend on external power sources such as batteries for powering that have a limited power budget and will make the system complex and bulkier. These issues could be addressed by using PVs. Because the PV current generated is proportional to the intensity of the incident light, a PV may also be utilized as a light sensor, which can then be used for detecting a shadow event such as gesture recognition. In addition, the PVs are self-powered due to energy harvesting and the surplus can be stored and utilized for operating other electronic components. Furthermore, by using the energy harvesters as sensors, space and resources may well be managed and deployed more effectively and efficiently.

**Figure 4** shows the response of fabricated OPV for various gestures at indoor ambient light conditions with 600 lux of LED illumination. The system consists of OPVs connected to a microprocessor through an analogue-to-digital converter, as

shown in the schematic in Figure 4a. The system was able to detect various hand gestures, including tapping and swiping (Figure 4b) and a demonstration of the functioning can be found in Movie S1, Supporting Information. The hand moves toward and away from a single OPV during the tapping operation, creating successive shadow instances. The measured voltage signals for single, two, and four tapings are demonstrated in Figure 4c. For swipe operation, two OPVs were employed and based on the hand motion, a shadow event travels from one OPV to another and the sequence of triggering defines the swipe direction (Figure 4d demonstrates the voltage signal for swipe operations). This approach can also be used to detect slippage during object manipulation. To evaluate the reliability of the OPVs for gesture recognition, a durability test was performed by performing 1000 swipe operations. Figure 4 e,f shows the initial and final 10 swipes, respectively (complete results are available in Figure S2, Supporting Information). The output voltage generated by OPV was observed to be stable throughout the cyclic operation, confirming good reliability of the OPVs for gesture-recognition applications.

### 2.2. Capacitive Touch Sensor Characterization

Various capacitive sensing structures, such as in-plane<sup>[34]</sup> and parallel plate electrode configurations,<sup>[35]</sup> have been explored in literature. In general, each of these structures consists of highly conducting electrode pairs with a dielectric in between the electrodes, and each of these materials needs to be transparent to realize a whole transparent sensor. In-plane capacitive sensors, consisting of electrode pairs on the same surface, are more popular due to their ease of fabrication, and high and uniform transparency. Minimal layer interfaces make the structure robust for mechanical flexibility and conformability. Here, we have fabricated in-plane interdigitated-electrode-based touch sensors using both ITO and graphene as the transparent electrodes. **Figure 5** shows the scanning electron microscope (SEM) image of the polyvinyl chloride (PVC) substrate (Figure 5a), graphene on Cu (Figure 5b), and after transferring the graphene from Cu to the PVC substrate by hot-roll processing (Figure 5c). The surface morphology of PVC was observed to be smoothed after the graphene transfer, and microstructural irregularity on the PVC surface disappeared. Some of the defective features on

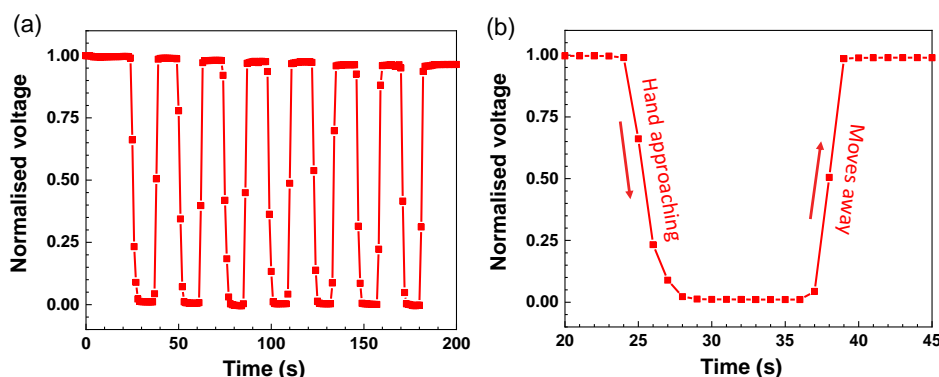


**Figure 3.** Proximity sensing using OPV. a) Cyclic repeatability of variation in photovoltage of OPV with object approaching the cell under 600 lux indoor illumination. b) The variation of photovoltage in the first cycle.

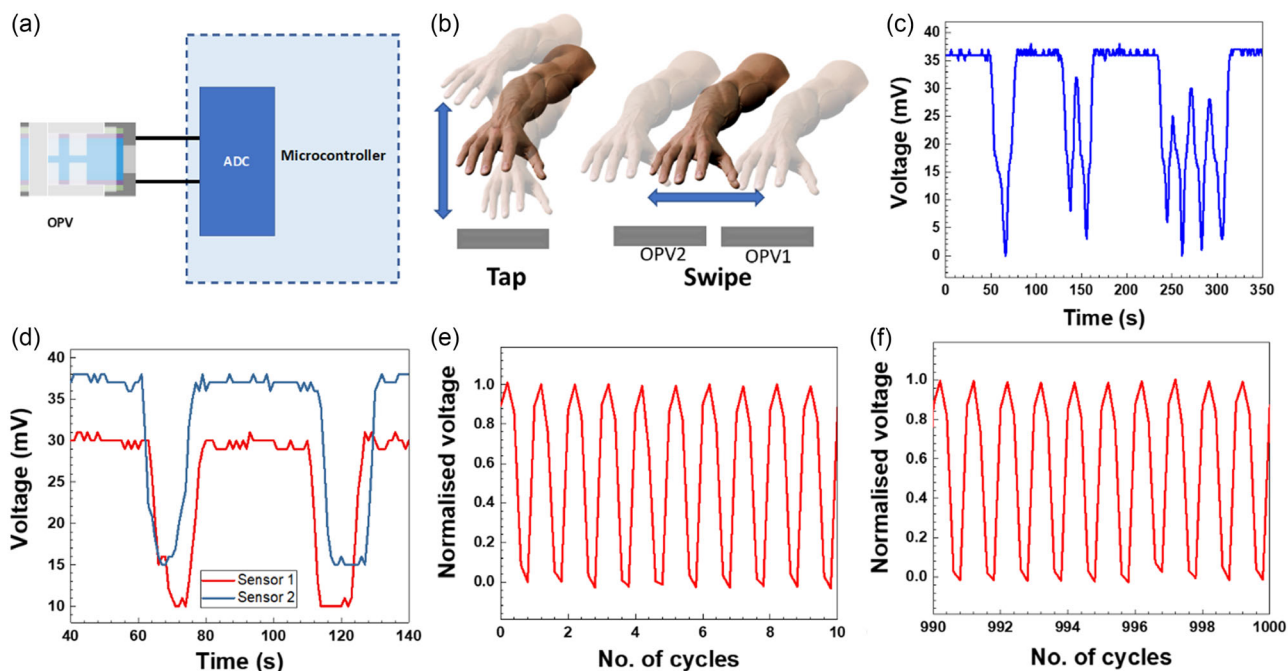


**Figure 4.** OPV-based gesture recognition. a) Schematic representation of the readout circuit for OPV-based sensing. b) Various gesture recognition such as multi-taps and swipe detection using OPV. c) The variation in the output voltage of OPV with multiple-tapping operations. d) The voltage signals corresponding to the right and left swipe operations were detected using two OPVs. Movie S1, Supporting Information, demonstrates the real-time monitoring of OPV-based gesture sensing. To evaluate the reliability of the OPVs for shadow sensing, a swipe operation was performed for 1000 times. The normalized voltage variations during the initial e) Ten cycles and f) final ten cycles confirm good reliability and durability of the OPVs for gesture recognition.

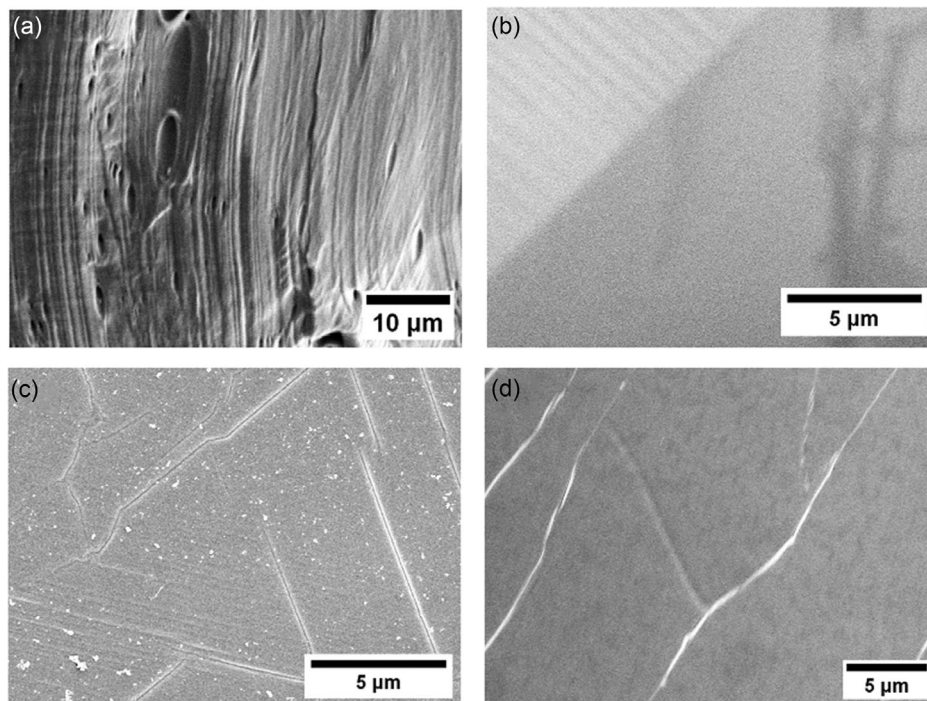


**Figure 5.** Morphology of the sensor electrodes. Scanning electron microscope (SEM) micrographs showing the surface morphology of the a) bare polyvinyl chloride (PVC) substrate, b) monolayer graphene on Cu foil, c) PVC surface after hot-roll transfer of graphene monolayer, and d) indium tin oxide (ITO)-coated polyethylene terephthalate (PET) sheet.

the graphene surface such as wrinkles and grain boundaries, that were visible in the graphene on Cu were also observed on the PVC surface after the hot-roll transfer, confirming the seamless transfer of the graphene during the process. Figure 5d shows the surface morphology of the ITO-coated PET sheet. Some microcracks are visible on the surface that can eventually affect the overall conductivity of the films and due to the brittle nature of the ceramic ITO, these cracks are expected to propagate further with mechanical bending and other deformations.

The transmittance spectra of ITO and graphene films are shown in Figure 6a. The ITO exhibited an overall transmittance of 91.2% while the monolayer graphene on PVC exhibited a transmittance of 85.6%, with respect to the ambient air. The transmittance also includes the effect of the plastic substrates. The ITO exhibited a better sheet resistance of  $100 \Omega \text{ sq}^{-1}$ . While the monolayer graphene exhibited  $5.4 \text{ k}\Omega \text{ sq}^{-1}$ . The electrical properties of graphene can be further enhanced by using multilayered graphene in future. To understand the mechanical durability of the electrodes, a bending test was performed at 5 mm bending diameter and the results are demonstrated in Figure 6b. The graphene electrodes exhibited better durability with minimal resistance variation after 1000 bending cycles, while the resistance of ITO-based electrodes was increased by up to eight times. Being ceramic, ITO is brittle in comparison to graphene and hence more susceptible to mechanical cracking and hence increases in the resistance. The interdigitated electrodes were patterned using a mechanical blade cutter.

Optical microscope images of the cuts on ITO and graphene electrodes are shown in Figure 6b,c, respectively.

Figure 7a shows the photograph of the fabricated transparent touch sensor using the ITO-based electrode. The Bendable Electronics and Sensing Technologies (BEST) logo kept at the bottom of the sensor is clearly visible, which confirms the optical transparency of the sensor. After the fabrication of the touch sensor, we studied the quasi-static pressure response of the touch sensors. To understand the performance of the sensors, both types of sensors were subjected to various pressure values, ranging from 0 to 60 kPa and their relative change in capacitance was measured, as shown in Figure 7b,c. When pressure is applied, the dielectric constant of PDMS varies under compression. The primary source of these dielectric variations is the increase in the volumetric density of the voids present in the cured PDMS.<sup>[9]</sup> The sensitivity ( $S$ ) of the sensors was extracted as

$$S = \frac{d((C - C_0)/C_0)}{dP} \quad (1)$$

where  $C_0$  is the initial capacitance without the applied pressure,  $P$ , and  $C$  is the final capacitance with the applied pressure,  $P$ . The ITO-based sensor exhibited a maximum response of  $0.255 \text{ kPa}^{-1}$  between 0 and 10 kPa pressure regime while the graphene-based sensor exhibited lesser but almost uniform sensitivity of  $0.006 \text{ kPa}^{-1}$  throughout the pressure range of 10–60 kPa. The ITO-based capacitive sensor exhibited higher capacitive change, especially in low-pressure regimes while the

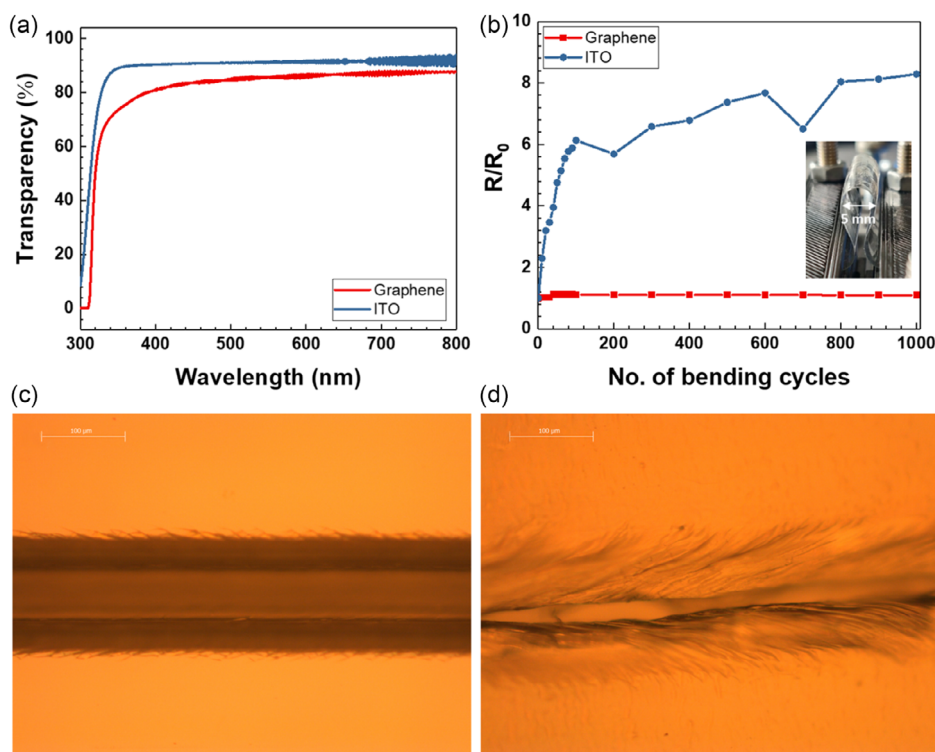


**Figure 6.** Properties of sensor electrodes. a) Optical transparency of transparent electrodes (ITO on PET sheet and monolayer graphene on PVC). b) The variation in the resistance of the electrode after 1000 bending cycles. Graphene-based electrode exhibited better stability against mechanical bending. Optical micrograph showing the longitudinal cuts on the c) ITO and d) graphene electrodes made using the blade cutter for patterning.

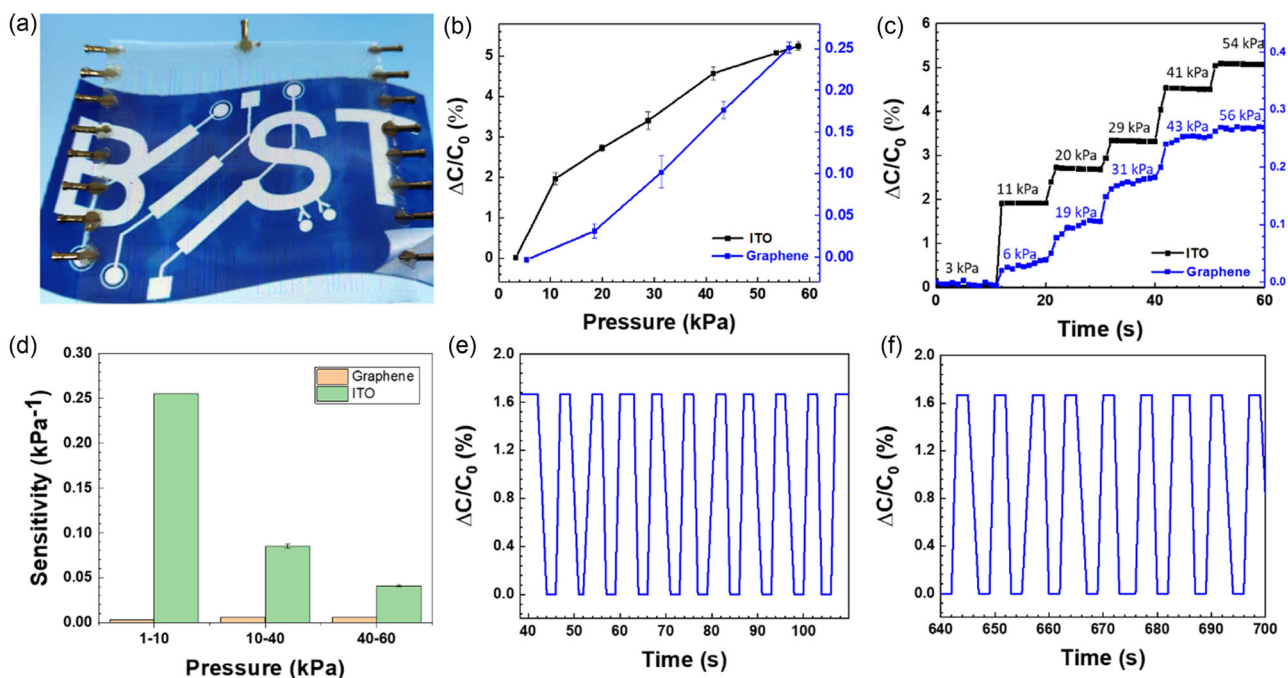


**Figure 7.** Performance of transparent capacitive touch sensors a) Photograph of the fabricated transparent touch sensor using ITO electrode. Clearly visible Bendable Electronics and Sensing Technologies (BEST) logo at the bottom of the sensor confirms the transparency. b) Step response of the touch sensors under various pressure values. c) Relative capacitance changes with respect to the applied pressure. ITO-based sensors exhibited better response compared to graphene. d) Comparison of the sensitivity of ITO and graphene sensors under various pressure regimes (1–10, 10–40, and 40–60 kPa). e) Initial and f) final cyclic response graph of the ITO-based pressure sensor during 500 cycles of  $\approx 8$  kPa loading.

graphene-based sensor exhibited a uniform response over a wide range of pressure regimes, as shown in Figure 7d. The excellent deformability of PDMS at low pressure causes a significant variance in capacitance. The elasticity of PDMS, in contrast, reaches its maximum in the high-pressure region  $>10$  kPa, leading to a modest capacitance change.

The long-term stability of the sensors was also evaluated using a cyclic load test, by subjecting the sensor to continuous loading and unloading of  $\approx 8$  kPa pressure at 0.25 Hz frequency for 500 cycles. The initial and final ten responses to the cyclic test were shown in Figure 7e,f, respectively. The response and recovery time of the sensors were observed to be quick, with  $<100$  ms. The sensor's performance was found to be steady, as evidenced by a comparable cyclic response at the start and end of the cyclic loading test, and hence the device is reliable for long-term use.

### 2.3. Stacked Integration of Touch Sensor with OPV

The transparency of touch sensors also makes it possible to obtain self-powered sensors. For this, the transparent touch sensors were integrated on the top of OPVs discussed earlier. The integration allowed both components to work without hindering the functionality of each other. Considering the potential use of OPVs as sensors, this integration will facilitate energy-autonomous tactile skins with extra sensing capabilities. While the touch sensors can detect any physical contact, the pressure applied and positioning information, the OPVs can also produce electricity from ambient light and provide shadow sensing,

including gesture-recognition capabilities as discussed before. As illustrated in the schematic, in Figure 8a, we developed a heterogeneous e-Skin stack employing OPV as the base and transparent touch sensors on top, as a solar skin or PV skin. Because it is the initial physical contact point, the top location of touch sensors ensures superior pressure detection. The intrinsic transparency of the individual layers used in the touch sensor, including the conducting electrodes (ITO or graphene), dielectric (PDMS), and substrate (PET or PVC), the light is expected to transmit through the sensor with minimal absorbance and reach the solar cell. After fabrication, the ITO-based touch sensor exhibited optical transparency of 73% while the graphene-based sensors exhibited 77% transmittance at 550 nm. Even though the results are contradictory to the electrode transparency shown in Figure 6a, the improved optical transparency of graphene-based touch sensors in comparison to ITO may be dominated by a superior PVC–PDMS optical interface, which results in low interface scattering and a reduction in PVC surface scattering owing to smoothing after PDMS coating.

To quantify how the OPV performance is affected by integration of touch sensor on top, the performance of the OPV was measured with different touch sensors integrated, as shown in Figures 8b,c, at a low light intensity of 600 lux. The  $V_{OC}$  and short-circuit current ( $I_{SC}$ ) were estimated from the current–voltage ( $I$ – $V$ ) characteristics and observed that both reduce after the integration of the sensors. This confirmed that the touch sensor is absorbing or/and reflecting some portion of the optical power as well as scattering at the interface might be another factor. The  $P_{MAX}$  of the OPV reduced to 79% after incorporating the

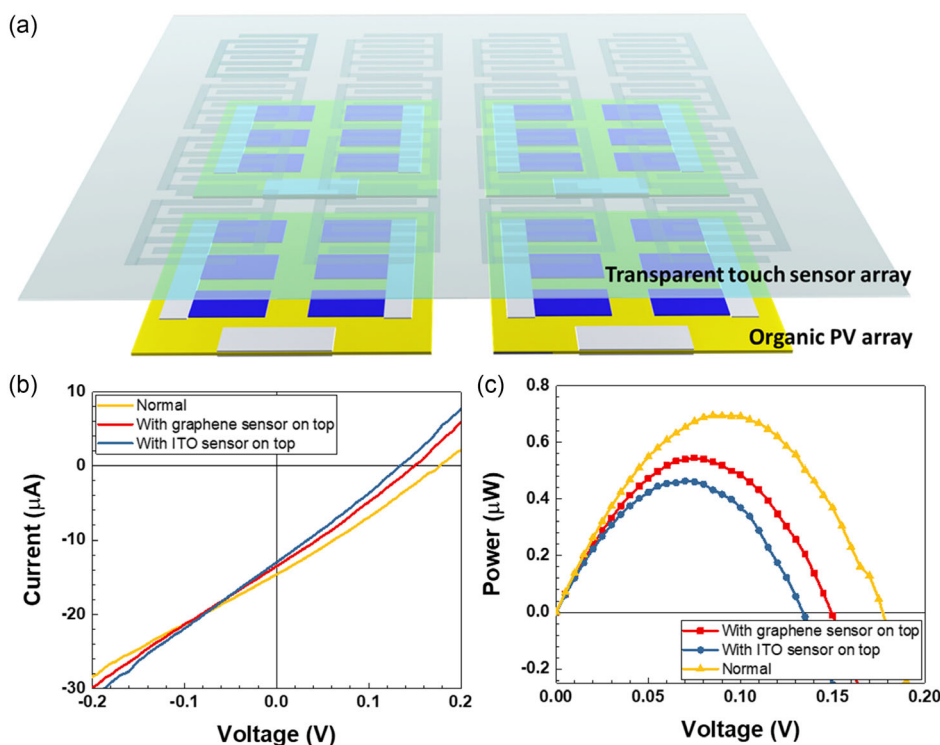


**Figure 8.** Stacked integration of touch sensor with OPV. a) Schematic showing the stack of pressure sensors with OPVs toward energy-autonomous e-Skin or solar skin. The variation in the performance of the OPV with transparent sensors installed on top; b)  $I$ - $V$  characteristics and c) power generated.

graphene sensor on top while it reduced further to 67% with the ITO sensor.

Finally, as proof of concept, a prototype solar or PV skin was developed with a  $2 \times 2$  array of touch sensors stacked on the OPV and the results are shown in **Figure 9** and Movie S2, Supporting Information. The outputs from OPVs and capacitive touch sensors were connected to the analogue pin of the Arduino UNO board for implementation. The fluctuation in voltage created by the OPV and the change in capacitance of the touch sensors were continuously monitored and serially transferred to a computer, where the data was further processed and displayed in real-time using Python code. To demonstrate any shadow casting and pressure, the point of touch is shown as a 3D bar chart, with the color of the chart adjusted dependent on the voltage created by OPV.

The presented capacitive touch sensor functions at  $1 V_{pp}$ , 500 kHz signal frequency, and it drains a current of  $0.5 \mu A$  during its operation, resulting in a power requirement of  $0.35 \mu W$  and a corresponding power density of  $\approx 0.25 \mu W cm^{-2}$ . The OPV utilized in this work can generate  $0.7 \mu W$  at 600 lux illumination, which corresponds to a power density of  $0.075 \mu W cm^{-2}$  after installing the ITO sensors on top (to also account for the implementation space constraints, the overall area of the OPV is considered instead of the effective area, which results in an underestimation of the generated power density). This means that the generated power density by OPV is not good enough to satisfy the power budget of the touch sensor at the lower illumination intensity. But, at higher illuminations of 1500 lux or higher, the same OPV can produce  $2 \mu W$  or more with a

corresponding minimum power density of  $0.32 \mu W cm^{-2}$ , as shown in Figure 2b,e, which is 28% in excess of the power required by the sensors. In a more realistic scenario, the e-Skins will be exposed to various illuminations ( $>10^4$  lux in at outdoor environment), where the excess generated power can be stored in a battery that can be utilized for the uninterrupted functioning of the e-Skin. The power usage efficiency can be further improved by implementing an event-driven strategy, where the touch-sensing layer will be powered only after a shadow event is detected by the OPV. In future, the OPV cells can be redesigned to improve the effective area together with enhanced electrical properties of the transparent electrodes to reduce the overall power budget of the touch sensors. The feasibility study in the current demonstration aims to show various uses of OPVs such as proximity and shadow detection along with the understanding of power management in energy-autonomous transparent e-Skin.

### 3. Conclusion

The current work demonstrated a heterogeneous integration of OPVs with transparent touch sensors to develop energy autonomous e-Skin that can “see” (e.g., approaching object through shadow sensing) and “feel.” The fabricated touch sensors that are placed on top of OPVs can identify a wider range of applied pressure and spatial touch information, and at the same time, being transparent, they allow the light to pass through them and reach the OPVs. Interdigitated electrodes of the touch



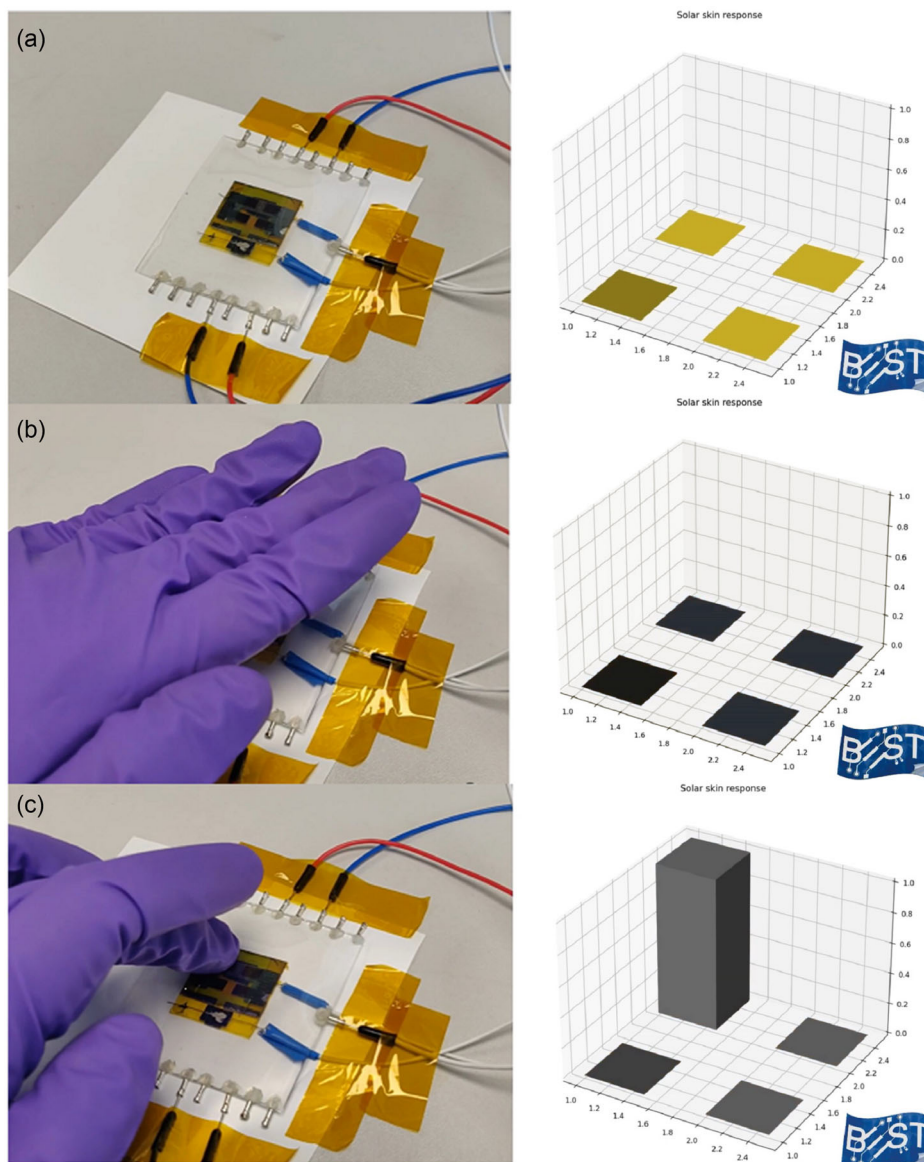


**Figure 9.** Working of the solar skin. Performance of the sensor stack under a) normal, b) shadow sensing, and c) touch-sensing modes of operations. The demonstration of the stack is available in Movie S2, Supporting Information.

sensors were fabricated by a simple mechanical blade cutter that supports swift large-area low-cost production. Both ITO and graphene were employed as touch sensor electrodes where ITO-based sensors exhibited better electronic properties, with better sensitivity below 10 kPa pressure, while the graphene was superior with optical transparency and mechanical flexibility. The OPV layer beneath the transparent touch sensor layer of the skin can function as both a power generator and as a shadow sensor for proximity and hand gesture recognition. In future, the OPV can be optimized further. For high-density imaging, the effective area needs to be reduced as it will improve the efficiency. The optoelectronic properties of the capacitive sensors can be boosted using composite materials for low-power sensing. The suggested e-Skin can mature into an energy-autonomous e-Skin with broad applications in robotics, prosthetics, health,

and wearable devices with improved resource use and localized power production.

#### 4. Experimental Section

**Materials:** ITO-coated PET sheets with  $>80\%$  transmittance and  $100\ \Omega\ \text{sq}^{-1}$  sheet resistance were purchased from Sigma Aldrich and was used as the electrodes for the sensor. Chemical vapor deposition (CVD)-grown monolayer graphene on Cu foil, purchased from ACS materials, was transferred to a  $125\ \mu\text{m}$  thick PVC sheet (Fellows gloss laminating pouch) by hot-roll transfer technique at  $125\ ^\circ\text{C}$ .<sup>[9]</sup> The Cu side was kept in contact with the paper to prevent lamination inside PVC. The Cu was then chemically etched by immersing it in 1 M  $\text{FeCl}_3$  solution for 2 h to complete the graphene on the PVC electrode.

**Sensor Fabrication:** Interdigitated electrode configurations were patterned over the electrode sheet (ITO and graphene) using a

computer-controlled precision cutting machine with a plotter blade, Silhouette Cameo 2. The cutting machine helps with complex patterning without the need for complex lithographic techniques or chemical etching procedures. The electrode was attached to a cutting mat for accurate positioning for patterning. The parameters such as blade height, cutting speed, and cutting force were optimized to get the sharp cuts needed to separate the conductive layer. PDMS (Sylgard 184), with part A and part B mixing in a 10:1 weight ratio, was spin-coated over the patterned electrodes and annealed at 90 °C for 60 min for the curing to form the dielectric coating. The OPV had a device structure of PET/ITO/ZnO/PTB7-th:PC<sub>71</sub>BM/MoO<sub>3</sub>/Ag, with an effective area of 1 cm<sup>2</sup> and a detailed description of their fabrication are available elsewhere.<sup>[36]</sup> PTB7-th and PC<sub>71</sub>BM layers were optimized slightly by changing the process parameter. The active layer thickness was tailored to be 80 nm using spin-coating and vacuum annealing. The fabricated OPV devices were encapsulated using PET films in an inert atmosphere to eliminate ambient air trapped inside the sealed device. The PET films were encapsulated to the device by a hermetic edge sealing technique<sup>[37]</sup> using UV curable (350–380 nm) epoxy (NOA 68). The edge sealant was cured for about 120 s at 4.5 J cm<sup>-2</sup>.

**Structural and Electrical Characterization:** The morphology of the films was characterized using a Leica optical microscope and Hitachi SU8240 SEM. The sheet resistance of the films was measured using an Ossila four-point probe measurement unit. Bending tests were performed using a custom-built setup, and in situ resistance was measured using a Keysight U3606B multimeter. The sensor performance was evaluated by applying force using a square-shaped plastic probe attached to a linear stage driven by a servomotor. The applied force was measured and calibrated using a load cell placed under the sensor. The output capacitance of the sensor was measured using a Keysight E4980AL precision LCR (inductance (L) capacitance (C) resistance (R)) meter and recorded using LabVIEW software. The OPVs were characterized using a Precision Source/Measure Unit B2912A (Keysight Technologies, Santa Clara, CA, USA). A white source LED with controllable intensity was used for illumination. The intensity of the LED was measured using the RS-9083 LED light meter purchased from RS-PRO.

## Supporting Information

Supporting Information is available from the Wiley Online Library or from the author.

## Acknowledgements

This work was supported by Engineering and Physical Sciences Research Council (EPSRC) through the Hetero-print Programme Grant (Grant no. EP/R03480X/1) and European Commission through FET-OPEN project Ph-Coding (Grant no. H2020-FETOPEN-2018-829186). The work in this article was started by R. Dahiya's Bendable Electronics and Sensing Technologies (BEST) Group, when he was in the University of Glasgow. The work was completed after he moved to Northeastern University, where his research group is known as Bendable Electronics and Sustainable Technologies (BEST) Group.

## Conflict of Interest

The authors declare no conflict of interest.

## Data Availability Statement

The data that support the findings of this study are available from the corresponding author upon reasonable request.

## Keywords

electronic skin (e-Skin), flexible electronics, graphene, indium tin oxide (ITO), organic photovoltaics, touch sensing, transparent electronics

Received: February 24, 2023

Revised: June 16, 2023

Published online: July 26, 2023

- [1] a) A. Paul, N. Yogeswaran, R. Dahiya, *Adv. Intell. Syst.* **2022**, *11*, 2200183; b) J. Neto, R. Chirila, A. S. Dahiya, A. Christou, D. Shakthivel, R. Dahiya, *Adv. Sci.* **2022**, *9*, 2201525; c) F. Liu, S. Deswal, A. Christou, Y. Sandamirskaya, M. Kaboli, R. Dahiya, *Sci. Robot.* **2022**, *7*, eabl7344; d) F. Nikbakhtnasrabadi, E. S. Hosseini, S. Dervin, D. Shakthivel, R. Dahiya, *Adv. Electron. Mater.* **2022**, *8*, 2101348.
- [2] R. Mukherjee, P. Ganguly, R. Dahiya, *Adv. Intell. Syst.* **2023**, *5*, 2100036.
- [3] a) A. H. Talkhooncheh, Y. Yu, A. Agarwal, W. W.-T. Kuo, K.-C. Chen, M. Wang, G. Hoskuldsdottir, W. Gao, A. Emami, *IEEE J. Solid-State Circuits* **2021**, *56*, 715; b) L. Yin, J.-M. Moon, J. R. Sempionatto, M. Lin, M. Cao, A. Trifonov, F. Zhang, Z. Lou, J.-M. Jeong, S.-J. Lee, S. Xu, J. Wang, *Joule* **2021**, *5*, 1888; c) L. Manjakkal, L. Yin, A. Nathan, J. Wang, R. Dahiya, *Adv. Mater.* **2021**, *33*, 2100899.
- [4] W. Navaraj, R. Dahiya, *Adv. Intell. Syst.* **2019**, *1*, 1900051.
- [5] A. Thakre, A. Kumar, H.-C. Song, D.-Y. Jeong, J. Ryu, *Sensors* **2019**, *19*, 2170.
- [6] G. Khandelwal, R. Dahiya, *Adv. Mater.* **2022**, *34*, 2200724.
- [7] Y. Du, J. Xu, B. Paul, P. Eklund, *Appl. Mater. Today* **2018**, *12*, 366.
- [8] C. García Núñez, L. Manjakkal, R. Dahiya, *NPJ Flexible Electron.* **2019**, *3*, 1.
- [9] C. G. Núñez, W. T. Navaraj, E. O. Polat, R. Dahiya, *Adv. Funct. Mater.* **2017**, *27*, 1606287.
- [10] L. Manjakkal, W. T. Navaraj, C. G. Núñez, R. Dahiya, *Adv. Sci.* **2019**, *6*, 1802251.
- [11] A. Varshney, A. Soleiman, L. Mottola, T. Voigt, in *Proc. of the 4th ACM Workshop on Visible Light Communication Systems*, Association for Computing Machinery, Snowbird, UT **2017**.
- [12] D. Ma, G. Lan, C. Hu, M. Hassan, W. Hu, U. Mushfika, A. Uddin, M. Youssef, in *IEEE Transactions on Mobile Computing, IEEE, Piscataway, NJ* **2022**, p. 1.
- [13] a) Y. Umetsu, Y. Nakamura, Y. Arakawa, M. Fujimoto, H. Suwa, in *IEEE Int. Conf. on Pervasive Computing and Communications (PerCom)*, IEEE, Piscataway, NJ **2019**; b) J. Randall, O. Amft, J. Bohn, M. Burri, *Pers. Ubiquitous Comput.* **2007**, *11*, 417.
- [14] P. Escobedo, M. Ntagios, D. Shakthivel, W. T. Navaraj, R. Dahiya, *IEEE Trans. Robot.* **2021**, *37*, 683.
- [15] M. Chakraborty, J. Kettle, R. Dahiya, *IEEE J. Flex. Electron.* **2022**, *1*, 4.
- [16] A. D. Rao, M. G. Murali, A. V. Kesavan, P. C. Ramamurthy, *Sol. Energy* **2018**, *174*, 1078.
- [17] L. Gao, L. Chao, M. Hou, J. Liang, Y. Chen, H. D. Yu, W. Huang, *NPJ Flexible Electron.* **2019**, *3*, 4.
- [18] a) N. M. Nair, M. M. Jahanara, D. Ray, P. Swaminathan, *Flexible Printed Electron.* **2021**, *6*, 045004; b) T. Y. Choi, B. U. Hwang, B. Y. Kim, T. Q. Trung, Y. H. Nam, D. N. Kim, K. Eom, N. E. Lee, *ACS Appl. Mater. Interfaces* **2017**, *9*, 18022.
- [19] N. M. Nair, I. Khanra, D. Ray, P. Swaminathan, *ACS Appl. Mater. Interfaces* **2021**, *13*, 34550.
- [20] a) O. Bierwagen, *Semicond. Sci. Technol.* **2015**, *30*, 024001; b) T. Minami, *Semicond. Sci. Technol.* **2005**, *20*, S35.

- [21] S. Bae, H. Kim, Y. Lee, X. Xu, J. S. Park, Y. Zheng, J. Balakrishnan, T. Lei, H. Ri Kim, Y. I. Song, Y. J. Kim, K. S. Kim, B. Özyilmaz, J. H. Ahn, B. H. Hong, S. Iijima, *Nat. Nanotechnol.* **2010**, *5*, 574.
- [22] N. Sharma, N. M. Nair, G. Nagasarvari, D. Ray, P. Swaminathan, *Flexible Print. Electron.* **2022**, *7*, 014009.
- [23] N. M. Nair, J. K. Pakkathillam, K. Kumar, K. Arunachalam, D. Ray, P. Swaminathan, *ACS Appl. Electron. Mater.* **2020**, *4*, 1000.
- [24] L. Song, W. Wang, E. Barabino, D. Yang, V. Korstgens, P. Zhang, S. V. Roth, P. Muller-Buschbaum, *ACS Appl. Mater. Interfaces* **2019**, *11*, 3125.
- [25] B. Usmani, R. Ranjan, S. Prateek, S. K. Gupta, R. K. Gupta, K. S. Nalwa, A. Garg, *Sol. Energy* **2021**, *214*, 220.
- [26] S. Mori, T. Gotanda, Y. Nakano, M. Saito, K. Todor, M. Hosoya, *Jpn. J. Appl. Phys.* **2015**, *54*, 071602.
- [27] S. Ryu, N. Y. Ha, Y. H. Ahn, J. Y. Park, S. Lee, *Sci. Rep.* **2021**, *11*, 16781.
- [28] M. Chegaar, A. Hamzaoui, A. Namoda, P. Petit, M. Aillerie, A. Herguth, *Energy Proc.* **2013**, *36*, 722.
- [29] M. Freitag, J. Teuscher, Y. Saygili, X. Zhang, F. Giordano, P. Liska, J. Hua, S. M. Zakeeruddin, J.-E. Moser, M. Grätzel, A. Hagfeldt, *Nat. Photonics* **2017**, *11*, 372.
- [30] M. Tan, J. Zhou, K. Xu, Z. Peng, Z. Ma, *IEEE Antennas Wirel. Propag. Lett.* **2020**, *19*, 705.
- [31] Y. Bai, L. Lu, J. Cheng, J. Liu, Y. Chen, J. Yu, *Comput. Netw.* **2020**, *181*, 107447.
- [32] R. Xie, J. Cao, *IEEE Sens. J.* **2016**, *16*, 4537.
- [33] a) Y. Zhou, G. Jiang, Y. Lin, *Pattern Recognit.* **2016**, *49*, 102; b) A. Christou, Y. Gao, W. T. Navaraj, H. Nassar, R. Dahiya, *Adv. Intell. Syst.* **2020**, *4*, 2000126.
- [34] a) N. M. Nair, K. Daniel, S. C. Vadali, D. Ray, P. Swaminathan, *Flexible Print. Electron.* **2019**, *4*, 45001; b) B. Porr, S. Daryanavard, L. M. Bohollo, H. Cowan, R. Dahiya, *PLoS One* **2022**, *17*, 0277974.
- [35] a) Y. Kumaresan, O. Ozioko, R. Dahiya, *IEEE Sens. J.* **2021**, *21*, 26243; b) M. Ntagios, R. Dahiya, *IEEE Sens. J.* **2022**, *1*, <https://doi.org/10.1109/JSEN.2022.3179233>.
- [36] A. V. Kesavan, A. D. Rao, P. C. Ramamurthy, *Org. Electron.* **2017**, *48*, 138.
- [37] a) V. Adiga, A. D. Rao, S. Kumar, S. Raghavan, P. C. Ramamurthy, *4th IEEE Int. Conf. on Emerging Electronics (ICEE)*, IEEE, Piscataway, NJ **2018**, p. 11; b) V. Adiga, B. Nath, P. C. Ramamurthy, D. R. Mahapatra, G. Hegde, in *IEEE 48th Photovoltaic Specialists Conf. (PVSC)*, IEEE, Piscataway, NJ **2021**; c) S. Seethamraju, S. Kumar, K. Bharadwaj B.G. Madras, S. Raghavan, P. C. Ramamurthy, *ACS Nano* **2016**, *10*, 6501.